


Article

Development of High-Performance Supercapacitor Electrodes Based on CeO₂/SiO₂/CMK-3 Composites

Chelliah Koventhan ^{1,2,†} , An-Ya Lo ^{1,2,*}, Chia-Chia Chang ^{2,†} and Ming-Liao Tsai ^{2,*}

¹ Institute of Electro-Optical Engineering, National Taiwan Normal University, Taipei 11677, Taiwan; koventhanc@ncut.edu.tw

² Department of Chemical Engineering and Materials Engineering, National Chin-Yi University of Technology, Taichung 411030, Taiwan; chia2831113@gmail.com

* Correspondence: aylo@ntnu.edu.tw (A.-Y.L.); mltsai@ncut.edu.tw (M.-L.T.)

† These authors contributed equally for this paper.

Abstract: A novel composite material consisting of cerium dioxide (CeO₂), silica (SiO₂), and mesoporous carbon (CMK-3) was developed for supercapacitor electrodes. The composite's synthesis involved a high-surface-area porous carbon combined with CeO₂ and SiO₂. The resulting material was characterized by a high specific capacitance due to its mesoporous structure and enhanced dispersion CeO₂ and SiO₂. The effects of different types of CeO₂ and SiO₂ are also discussed. Both CeO₂ and SiO₂ components offer advantages such as abundance, low costs, and excellent catalytic properties. The composite's structure improves CeO₂ nanofiber (CeO₂ NF) dispersion and reduces impedance through rapid redox reactions. The influence of the CeO₂/SiO₂/CMK-3 ratio on specific capacitance was investigated. The optimized composite electrode demonstrated a significantly improved specific capacitance, 2.6 times higher than that of the pristine mesoporous carbon electrode. This work highlights the potential of CeO₂/SiO₂/CMK-3 composites for energy storage applications and underscores the importance of optimizing component ratios and morphology for improved supercapacitor performance.

Keywords: mesoporous carbon; supercapacitor; cerium dioxide (CeO₂); CMK-3; SiO₂



Academic Editors: Shamim Ahmed Hira and Antony R. Thiruppathi

Received: 9 April 2025

Revised: 24 May 2025

Accepted: 29 May 2025

Published: 3 June 2025

Citation: Koventhan, C.; Lo, A.-Y.; Chang, C.-C.; Tsai, M.-L. Development of High-Performance Supercapacitor Electrodes Based on CeO₂/SiO₂/CMK-3 Composites. *Processes* **2025**, *13*, 1766. <https://doi.org/10.3390/pr13061766>

Copyright: © 2025 by the authors. Licensee MDPI, Basel, Switzerland. This article is an open access article distributed under the terms and conditions of the Creative Commons Attribution (CC BY) license (<https://creativecommons.org/licenses/by/4.0/>).

1. Introduction

With the continuous rise in global energy demand, the development of clean and sustainable energy technologies is critical to reducing the environmental impact of conventional fossil fuels and meeting the growing need for efficient energy storage systems. Supercapacitors, energy storage devices bridging the gap between batteries and conventional capacitors [1,2], are poised to replace these technologies in certain applications. Their high power density, long cycle life, and rapid charge–discharge characteristics make them highly attractive. Further enhancing their energy density will unlock broader applications in areas such as electric vehicles, portable electronics, and renewable energy systems. Achieving this requires a focus on enhancing the energy density of supercapacitors while maintaining their essential advantages. A key strategy in approaching this challenge is the development of composite electrode materials with high specific capacitance and stability [3].

Carbon-based materials are widely used in electric double-layer capacitors (EDLCs) due to their high surface area, conductivity, and thermal/chemical stability. These materials, derived from abundant and sustainable sources, offer low costs and are industrially relevant. In EDLCs, energy is stored by electrostatic charge accumulation at the electrode–electrolyte

interface rather than by Faradaic processes. Some examples include activated carbon (AC) [4,5], carbon nanofibers [6,7], carbon nanotubes (CNTs) [8–11], graphene [6,11,12], carbide-derived carbon [13], and mesoporous carbon [14], which have attracted significant attention. Mesoporous carbon is of particular interest due to its high and stable surface area for charge storage. This high surface area not only enhances double-layer capacitance but also makes mesoporous carbon a suitable host for electroactive nanoparticles, thereby enabling a synergistic effect through additional Faradaic contributions [14,15].

In contrast to traditional capacitors, pseudocapacitors offer a battery-like energy storage mechanism [16], relying on fast, reversible Faradaic redox reactions between the electrode and electrolyte (e.g., OH^- , H^+) during charge–discharge [1]. These reactions can either be surface-controlled (pseudocapacitance) or diffusion-controlled (battery-type behavior), contributing to higher energy densities than EDLCs [17]. However, Faradaic electrode materials also exhibit faster electrode degradation, lower stability and cycle life due to their use of active materials, and lower charge–discharge efficiency, resulting in longer charging times. Faradaic electrode materials fall into three main categories: conductive polymers, transition metal oxides, and other materials (metal hydroxides, sulfides, nitrides, etc.) [1,5,15]. Conductive polymers include polyaniline (PANI), polypyrrole (PPy), and poly(3,4-ethylenedioxythiophene) (PEDOT), which are widely studied for their good electrical conductivity and flexibility [15,18,19]. Transition metal oxide research, initially focused on RuO_2 with its high theoretical capacitance ($>700 \text{ F/g}$) [20], has shifted towards lower-cost materials due to the high cost and scarcity of ruthenium [21]. These materials include manganese oxides (MnO_2 , Mn_3O_4) [22,23], cobalt oxides [24], iron oxides (Fe_2O_3) [21,25], tin oxides (SnO_2) [26], and spinel oxide [27]. Other promising materials include nickel hydroxide (Ni(OH)_2) [28], cobalt sulfide (CoS) [29], titanium nitride (TiN) [30], and tungsten nitride (W_2N) [31]. Beyond symmetric EDLCs and Faradaic-type capacitors, hybrid supercapacitors have emerged in recent years, combining the advantages of both [8,10,11,15,32]. These devices utilize both double-layer capacitance and Faradaic reactions during charge–discharge processes, resulting in a high power density and increased operating voltage, leading to enhanced energy density [18,32]. This has attracted significant research interest.

Transition metal oxides have become a focal point in supercapacitor electrode research due to their Faradaic reaction characteristics [33]. Cerium oxide (CeO_2), a typical rare earth oxide, has garnered attention for its unique redox properties [34]. Composites of CeO_2 with other metal oxides or carbon materials can enhance electrochemical activity. The rapid redox reactions between Ce(III) and Ce(IV) during electrode charge–discharge increase conductivity while maintaining the original fluorite structure [35,36]. CeO_2 's fast, reversible redox reactions and oxygen vacancies enhance its conductivity and electrochemical activity [34]. However, CeO_2 also has limitations, such as low conductivity and a tendency to agglomerate, restricting its application in supercapacitor electrodes. To address these limitations, researchers often combine CeO_2 with highly conductive materials like carbon or conductive polymers to improve conductivity and dispersion [37], thereby enhancing overall supercapacitor performance.

In this study, ordered mesoporous carbon CMK-3 was selected as the substrate material, and its high specific surface area and regular pore structure were adopted to disperse and support CeO_2 NFs. The influence of the $\text{CeO}_2/\text{SiO}_2/\text{CMK-3}$ ratio on specific capacitance was investigated. The optimized composite electrode demonstrated an easy and cost-efficient strategy as a reference for the future design of supercapacitor electrodes.

2. Materials and Methods

2.1. SBA-15 and CMK-3 Preparation

Mesoporous carbon CMK-3 was synthesized using a nanocasting technique, employing mesoporous silica (SBA-15) as a rigid template [14,38]. The SBA-15 template was initially created following a well-established protocol. This involved dissolving the triblock copolymer P123 ($\text{EO}_{20}\text{-PO}_{70}\text{-EO}_{20}$; Pluronic P123; Sigma-Aldrich, St. Louis, MI, USA) and tetraethyl orthosilicate (TEOS; Sigma-Aldrich, USA) in a hydrochloric acid solution (1.3 M) under continuous stirring at 40 °C. The resulting white SBA-15 material was then obtained through a process of aging in an oven (373 K for 48 h), followed by filtration and washing using a Büchner funnel, oven drying, and calcination in a furnace at 843 K for 6 h.

Subsequently, a solution of sucrose ($\text{C}_{12}\text{H}_{22}\text{O}_{11}$, Showa Chemical Co., Ltd., Tokyo, Japan) and sulfuric acid (H_2SO_4 , Showa Chemical Co., Ltd., Japan) in water was introduced dropwise to the SBA-15 template. The weight ratio of SBA-15 to sucrose to H_2SO_4 to water was maintained at 1/1.25/0.14/5. The mixture then underwent a heat-treatment process, involving 6 h at 60 °C followed by 6 h at 120 °C, to facilitate dehydration. This sucrose impregnation and heat-treatment cycle was repeated once to ensure the thorough filling of the SBA-15 channels.

Following this, the material was subjected to high-temperature carbonization at 900 °C under an inert atmosphere. Finally, the silica template was selectively removed by treatment with a 1.0 M hydrofluoric acid (HCl; Showa Chemical Co., Ltd., Japan) solution. The resulting mesoporous CMK-3 was then collected by filtration, washed extensively on a Büchner funnel, and dried in an oven.

2.2. CeO_2 Microparticle and CeO_2 Nanofiber Preparation

The preparation of CeO_2 microparticles (CeO_2 MPs) was based on and modified from the method described by Prasanna et al. [39]. Cerium (III) nitrate hexahydrate ($\text{Ce}(\text{NO}_3)_3 \cdot 6\text{H}_2\text{O}$; Alfa Aesar, Ward Hill, MA, USA) and glycine ($\text{C}_2\text{H}_5\text{NO}_2$; Alfa Aesar, USA) were used as starting materials, with a ratio of cerium nitrate/glycine/water = 5 mmol:25 mmol:30 mL. The mixture was combusted in a reactor at 300 °C for 5 min. After naturally cooling to room temperature, the sample was repeatedly filtered and washed with deionized water and absolute ethanol. The precipitate was dried at 80 °C and then calcined at 600 °C for 4 h to obtain CeO_2 MPs.

The preparation of CeO_2 NFs was based on and modified from the method described by Xu et al. [39]. Firstly, 5.88 g of sodium citrate ($\text{Na}_3\text{C}_6\text{H}_5\text{O}_7$; Showa Chemical Co., Ltd., Tokyo, Japan) was dissolved in 80 mL of deionized water and stirred uniformly for 10 min. Then, 2.4 g of urea ($\text{CO}(\text{NH}_2)_2$; Showa Chemical Co., Ltd., Japan) was added and stirred until combined. Subsequently, a prepared cerium nitrate solution (1.63 g of cerium nitrate dissolved in 20 mL of deionized water) was added dropwise and stirred uniformly for 30 min until the liquid turned pale yellow. The mixture was then placed in a Teflon-lined autoclave and subjected to hydrothermal reaction at 120 °C for 39 h. After naturally cooling to room temperature, the precipitate was collected by filtration, washed several times with deionized water and an ethanol–water solution, and then calcined at 500 °C in air for 4 h to obtain broom-like aggregates of CeO_2 NFs.

2.3. Electrode Preparation

The prepared materials (SiO_2 , SBA-15, CeO_2) and Super-P were dissolved separately in N-methylpyrrolidone (NMP; Echo Chemical Co., Ltd., Tainan, Taiwan). After pre-treatment with stirring and sonication, 0.04 g of CMK-3, 0.1 g of 5% Polyvinylidene difluoride (PVDF; Sigma-Aldrich, St. Louis, MA, USA), and an appropriate amount of NMP were added to the sample bottle. The mixture was repeatedly stirred and sonicated twice at room

temperature. The resulting black viscous liquid was used as the slurry for the electrode film. Next, a titanium sheet was used as the substrate (Area $2 \times 1 \text{ cm}^2$), and the slurry was uniformly coated onto it. The coated substrate was placed in a vacuum oven and dried at 100°C for 30 min. After removing the substrate, excess slurry was wiped off with acetone to obtain the electrode, with the loading mass varying for each electrode.

2.4. Analysis Methods

The synthesized CeO_2 and $\text{CeO}_2/\text{CMK-3}$ composite electrode materials were characterized using Scanning Electron Microscopy (SEM; JEOL JSM-7610F, JEOL Ltd., Tokyo, Japan), Transmission Electron Microscopy (TEM; JEOL JEM-2100, JEOL Ltd., Japan), X-ray Diffraction (XRD; PANalytical X'Pert PRO, Malvern Panalytical, Almelo, The Netherlands), and Brunauer–Emmett–Teller (BET; Micromeritics ASAP 2020, Micromeritics Instrument Corp., Norcross, GA, USA) methods. These techniques were used to analyze the materials' microstructure, including morphology, crystal structure, specific surface area, and pore size distribution. In addition, contact angle measurements were performed to assess the hydrophilicity of the materials. Electrochemical testing was performed using a three-electrode setup, consisting of platinum wire counter electrodes, Ag/AgCl reference electrodes, and a 1 M sulfuric acid electrolyte (H_2SO_4). Galvanostatic Charge–Discharge (GCD) and electrochemical impedance spectroscopy (EIS) measurements (potentiostat CHI 6273E; manufactured by CH Instruments, Bee Cave, TX, USA) were used to evaluate the capacitive performance, cycle stability, and charge transfer resistance of the electrode materials. The GCD tests were conducted at different current densities (1–50 A/g) within a potential range of 0.0 to 1.0 V (vs. Ag/AgCl), and the specific capacitance, energy density, and power density were calculated using the following equations:

$$C_g = j \int \frac{dt}{U(t)} \quad (1)$$

$$E = \frac{1}{2} C_g \Delta V^2 \quad (2)$$

$$P = \frac{E \times 3600}{\Delta t} \quad (3)$$

where C_g is the gravimetric electrode capacitance (F/g), j is the applied current density, dt is the discharge time, $U(t)$ is the potential as a function of time, E is the specific energy (Wh kg^{-1}), ΔV is the potential window (V), P is the specific power (W kg^{-1}), and Δt is the discharge time (s).

3. Results and Discussion

3.1. Material Characterization

Figure 1a–d show the SEM images of the SBA-15, CMK-3, CeO_2 MPs, CeO_2 NFs, and SiO_2 nanospheres (100 and 200 nm) synthesized in this study. Figure 1a,b show that we successfully fabricated CMK-3 with a similar microscopic morphology to SBA-15. Figure 1c,d show that we successfully synthesized CeO_2 MPs and CeO_2 NFs. The CeO_2 NFs exhibit a large number of nanoscale structures and are self-assembled from small nanorods into larger aggregates, which is expected to effectively increase their active surface area. The morphology and dispersion of the SiO_2 nanospheres (100 nm and 200 nm) are presented in (Figure S1). The SEM images reveal that the SiO_2 nanospheres exhibit a uniform spherical shape with a distinct size distribution. The presence of these nanospheres is expected to provide a well-defined surface area that may enhance the electrode–electrolyte interaction. According to the literature, this complex nanostructure will also help to improve its electrochemical activity. Figure 2a–c show the 77 K nitrogen

adsorption–desorption isotherms of the SBA-15, CMK-3, CeO₂ MPs, and CeO₂ nanofiber precursors synthesized in this study. Based on these isotherms, we obtained their specific surface areas, which were 796, 1254, 22, and 56 m²/g, respectively. SBA-15 and CMK-3 have high specific surface areas, similar to those reported in the literature. The CeO₂ NFs have a significantly higher specific surface area than the CeO₂ MPs, which is closely related to their unique morphology. Figure 3a shows the typical ordered mesoporous structure of SBA-15 and CMK-3, while Figure 3b shows that both types of CeO₂ have a cubic fluorite structure. The full width at half maximum (FWHM) of the XRD characteristic peak of the CeO₂ NFs is much wider than that of the CeO₂ MPs. This peak broadening can be attributed to the nanoscale nature of the particles. According to Scherrer's equation, the calculated crystallite sizes are 4.6 nm for CeO₂ NFs and 5.2 nm for CeO₂ MPs, confirming their distinct structural characteristics. In the CeO₂ NFs/SiO₂/CMK-3 composite (Figure S2), the addition of SiO₂ nanospheres further affects the structural properties, resulting in slightly broader peaks compared to CeO₂ MPs. This broadening suggests a decrease in crystallite size and the presence of additional lattice defects, which can enhance electrochemical performance. The combination of nanoscale CeO₂, well-dispersed SiO₂, and the conductive CMK-3 matrix provides a synergistic effect, leading to better electrochemical properties.

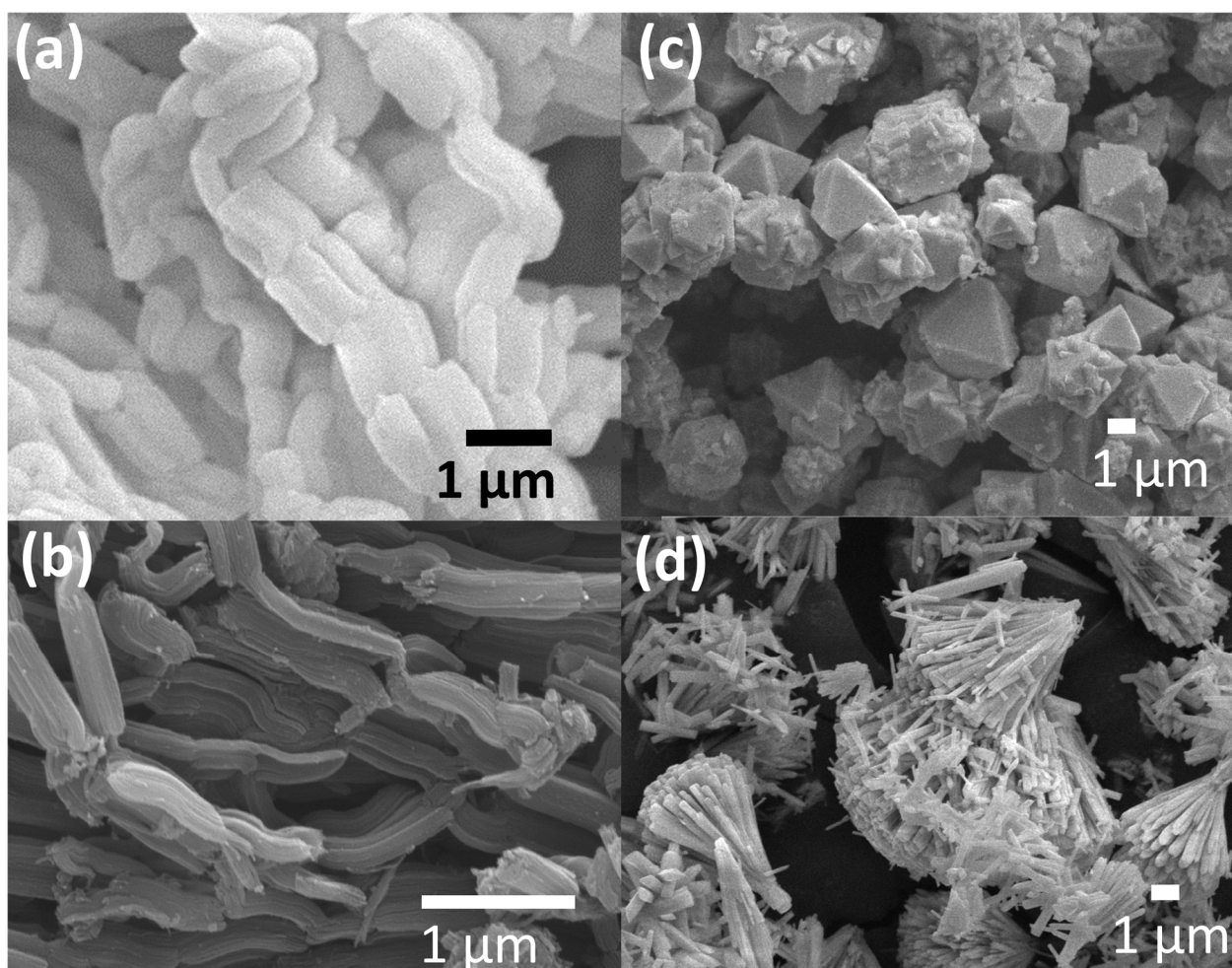


Figure 1. SEM images of (a) SBA-15, (b) CMK-3, (c) CeO₂ MPs, and (d) CeO₂ NFs synthesized in this study.

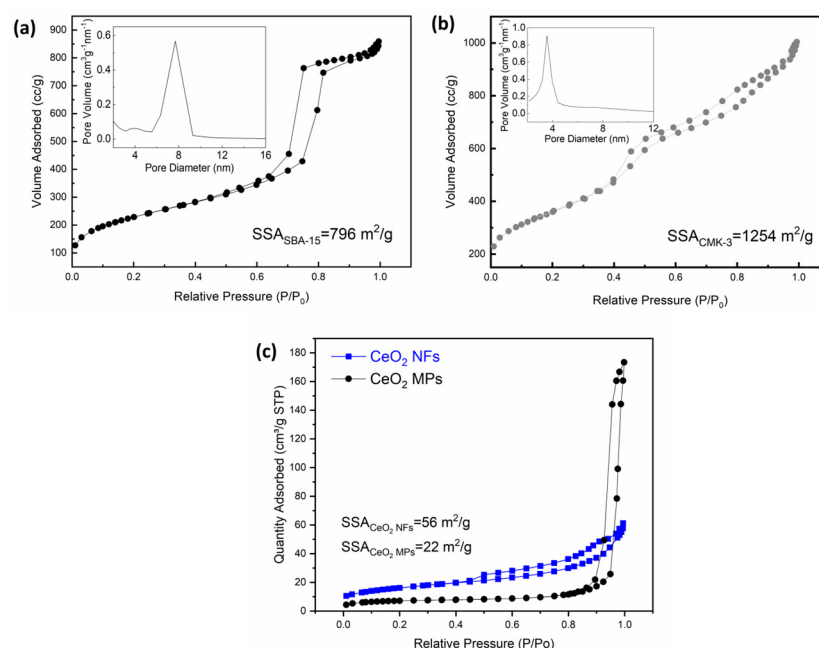


Figure 2. BET nitrogen adsorption–desorption isotherms recorded at 77 K for synthesized porous materials: (a) SBA-15, (b) CMK-3, (c) CeO₂ MPs and CeO₂ NFs.

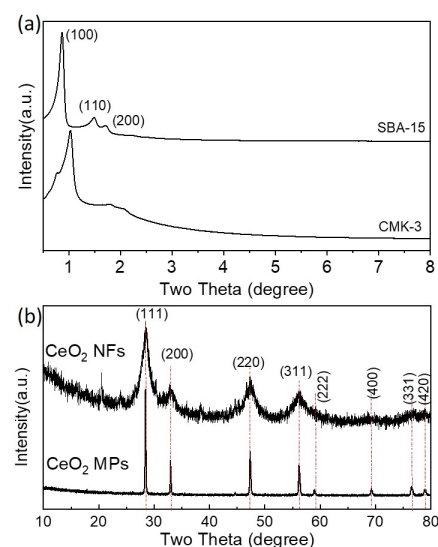


Figure 3. (a) Low-angle XRD indicating ordering mesoporous structure of SBA-15 and CMK-3; (b) XRD patterns showing cubic fluorite structure of both CeO₂ MPs and CeO₂ NFs.

3.2. Selection of Silica Materials

In the past, we found that adding hydrophilic silica nanospheres effectively increased the specific capacitance of electrode materials. Because SiO₂ is an insulator, we attributed the increase in capacitance to its hydrophilicity, which improves the interfacial affinity between the electrolyte and the composite electrode. Here, we replaced the added material with mesoporous silica material SBA-15, which has a better water absorption capacity, to investigate the effect of different addition ratios on the capacitance value.

Figure S3 shows the charge–discharge curves for SBA-15 addition ratios of 1%, 2%, 4%, 6%, 8%, 10%, and 15% at 1 A/g. The obvious IR drop and the resulting highly asymmetric charge–discharge curves indicate that the performance of the composite electrode is not ideal. For ease of comparison, Figure 4a shows the trend of the SBA-15 ratio versus specific capacitance from Figure S3. The measured capacitance values are all lower than that of

the original CMK-3. In addition, the specific capacitances of the composite electrodes with 1%, 2%, 4%, 6%, 8%, 10%, and 15% SBA-15 are 121.37 F/g, 66.9 F/g, 91.18 F/g, 71.3 F/g, 49.1 F/g, 105.47 F/g, and 58.3 F/g, respectively (Figure 4a). The lack of a clear trend in the capacitance change suggests that it may be difficult to achieve uniform and stable dispersion and quality in SBA-15/CMK-3 composite electrodes. This indirectly explains why the capacitance value does not increase but decreases. Because there is no obvious correlation between the amount of SBA-15 added and the specific capacitance, this is consistent with our past observations of 50 nm and 400 nm SiO₂ microspheres, suggesting poor dispersion in the electrode material. Due to the large size of SBA-15 (approximately 500 nm wide) and its long, lotus-root-like structure, it tends to aggregate severely. Analysis of Figure 4b,c shows that SBA-15 is severely agglomerated in the composite electrode. Therefore, the SBA-15/CMK-3 electrode material not only fails to effectively improve the electrochemical performance but also exhibits the excessive agglomeration of 50 nm silica spheres and structural collapse caused by 400 nm silica spheres.

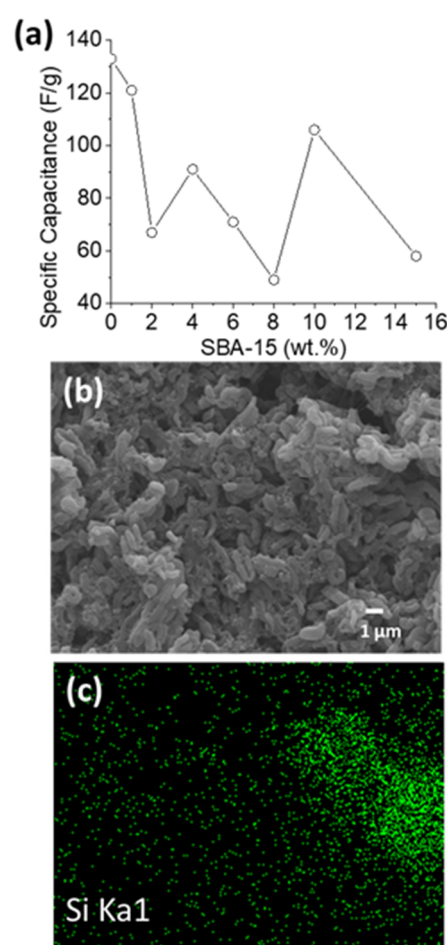


Figure 4. (a) Effect of different SBA-15 ratios on capacitance values; (b,c) SEM images and silicon elemental mapping of SBA-15/CMK-3 composite electrode.

The water contact angle test (Figure S4) confirms the superior hydrophilicity. On the other hand, it also allows further speculation about uneven SBA-15 distribution. Because the material itself has very good water absorption properties, the droplets on some samples are quickly absorbed after contacting the surface, making it impossible to effectively measure the contact angle. However, in the 4%, 8%, and 15% electrode sheets, it was found that the droplets were not directly absorbed, so it was judged that the absorption should depend

on the proportion of SBA-15 at that point. Therefore, the lack of trend in the capacitance value in Figure 4a is also attributed to the uneven distribution of the material.

3.3. Selection of CeO_2 Material

3.3.1. CeO_2 MPs/CMK-3 Composite Electrode

To investigate the effect of the addition amount on the capacitance value, different ratios (30%, 40%, 60%, 70%) of CeO_2 MPs were added to CMK-3 to form composite electrode materials. After three cycles of testing at a current density of 1 A/g, the charge–discharge curves are shown in Figure S5. Figure 5a shows the capacitance values obtained from Figure S5, which are 151.86 F/g, 159.66 F/g, 216.85 F/g, 163.56 F/g, and 153.16 F/g, respectively. It can be seen that the capacitance value changes with the amount of CeO_2 added. When the addition amount increases from 30% to 50%, the capacitance value shows the expected gradual upward trend, reaching a maximum value at 50% addition. However, if the addition amount is further increased, the capacitance value decreases.

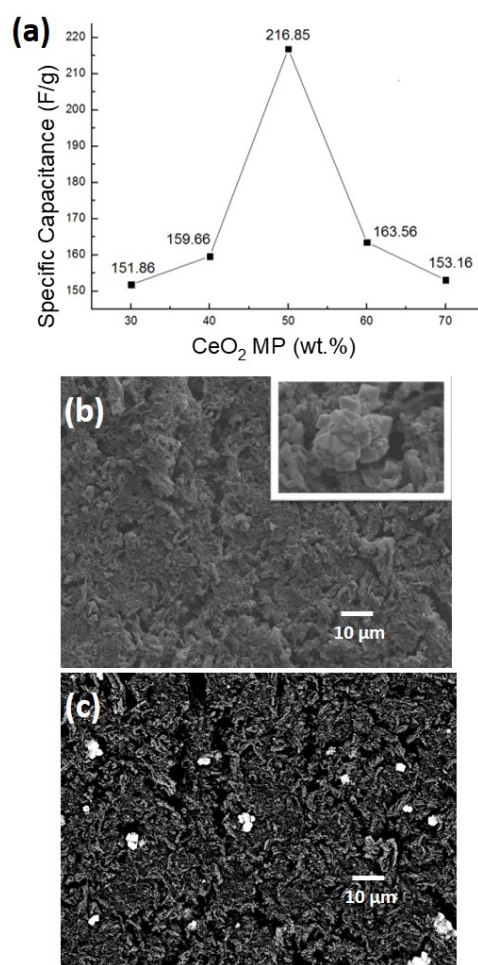


Figure 5. (a) Effect of CeO_2 MP loading on capacitance values; (b) SEM secondary electron image of composite electrode (inset: magnified view); (c) SEM backscattered electron image of composite electrode.

Figure 5b shows the SEM secondary electron microscopic image of the composite electrode. However, secondary electron images are not conducive to distinguishing the elemental distribution of carbon and Ce. Therefore, the backscattered electron imaging technique, shown in Figure 5c, was used to clearly distinguish the distribution of cerium oxide in the material. The EDX analysis (Figure S6a) further confirms the presence and distribution of Ce, C, and O. Additionally, the EDX spectrum reveals the presence of residual

precursors or synthesis reagents, as well as Pt signals originating from the sputtering for SEM. It can be observed that the particles tend to aggregate. Therefore, under the condition of excessive content, the electrochemical properties of the electrode material cannot be improved.

3.3.2. CeO₂ NFs/CMK-3 Composite Electrode

Under the same addition conditions (30%, 40%, 50%, 60%, 70%), the cerium oxide was replaced with CeO₂ NFs possessing a nanostructure in order to compare the effect of morphology on the capacitance value. Figure S7 and Figure 6a show the measured capacitance values at 1 A/g, which are 207.75 F/g, 248.64 F/g, 298.38 F/g, 219.25 F/g, and 208.65 F/g, respectively.

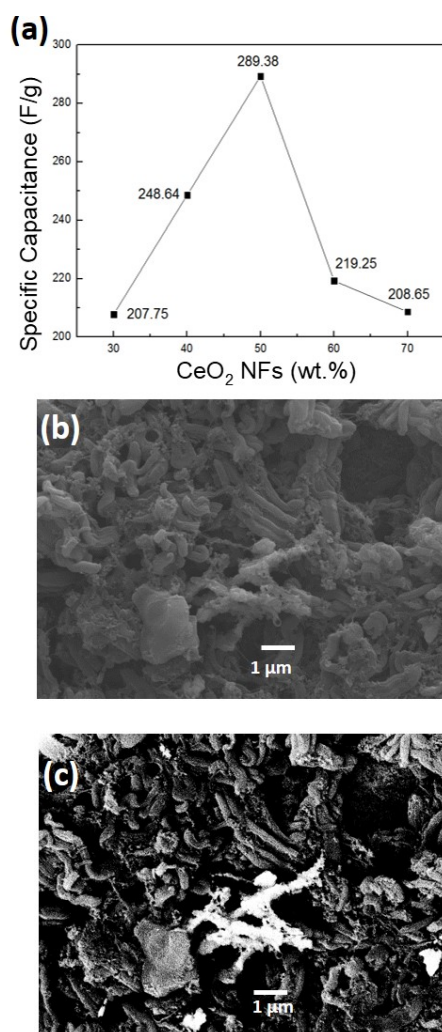


Figure 6. (a) The effect of the loading of CeO₂ NFs on capacitance values for the CeO₂ NFs/CMK-3 composite electrode; (b) the SEM image of the CeO₂ NFs/CMK-3 composite electrode; (c) the SEM backscattered electron image of the CeO₂ NFs/CMK-3 composite electrode.

Compared with the CeO₂ MPs (Figure 5a), Figure 6a shows a similar trend. When the addition amount is excessive, the aggregation phenomenon hinders electron transport and reduces its electrochemical performance. Figure 6b,c show the SEM secondary electron and backscattered electron microscopic images of the composite electrode, respectively. It can be clearly seen that the cerium oxide at this point maintains good dispersion. Further, the EDX analysis (Figure S6b) confirms the elemental percentage. The ultrasonic vibration and stirring pre-treatment in the process is an important step to make the aggregated nanorods

disperse evenly. This also makes the overall capacitance performance of the CeO_2 NFs better than that of the CeO_2 MPs.

In summary, if the cerium oxide is controlled within a certain ratio, the effect it brings is significant. Compared with pure carbon materials, the contribution to the capacitance value is greater than 150 F/g when 50% is added.

3.4. Electrochemical Properties of CeO_2 NFs/ SiO_2 /CMK-3 Ternary Composite Electrode

To further improve performance, and building upon our previous research [14], we used the optimal conditions for capacitance performance (50% CeO_2 NFs/CMK-3) and added different ratios of 100 nm and 200 nm silica spheres to investigate the specific capacitance at 1 A/g of the ternary composite material. The morphology and dispersion of the CeO_2 NFs/ SiO_2 -100 nm/CMK-3 and CeO_2 NFs/ SiO_2 -200 nm/CMK-3 composites were examined. The SEM images (Figure S8) reveal that both the 100 nm and 200 nm SiO_2 spheres exhibit uniform spherical shapes and are well distributed within the composite matrix. However, the 100 nm SiO_2 spheres demonstrate a more homogeneous dispersion compared to the 200 nm spheres, resulting in a more interconnected structure that could facilitate ion transport and enhance electrochemical performance. Further, EDX analysis confirms the presence of Si, Ce, and C, verifying the successful incorporation of both silica and cerium oxide within the CMK-3 matrix. Figure S9 shows the charge–discharge curves with varying amounts of 100 nm and 200 nm silica spheres when the CeO_2 NFs/CMK-3 ratio is 1:1. The trend of capacitance change is summarized in Figure 7. Both the 100 nm and 200 nm silica spheres achieve the best specific capacitance at a content of 4%, and the effect of the 100 nm silica spheres is better than that of the 200 nm silica spheres. This is consistent with the trend of our previous research on SiO_2 /CMK-3 composite electrodes [14]. When the silica particle size is 200 nm, the capacitance value of the ternary composite electrode is significantly improved compared to the binary composite, reaching 324 F/g. When the silica particle size is reduced to 100 nm, the electrode capacitance value of the ternary composite material is greatly improved, and the measured capacitance value is 403 F/g. This capacitance contribution is attributed to the synergistic effect produced by the simultaneous addition of cerium oxide and silica. It not only helps ion transport through the hydrophilicity of silica but also improves electron conductivity through the redox properties of cerium oxide [34].

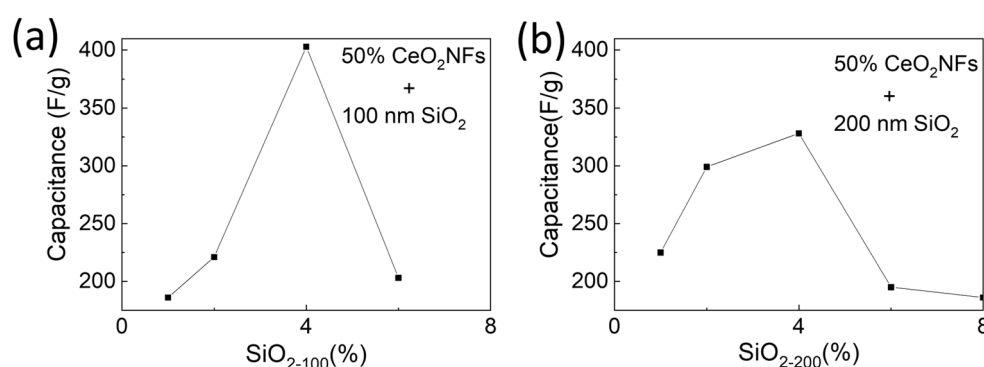


Figure 7. Effect of (a) 100 nm and (b) 200 nm silica sphere additives on specific capacitance of CeO_2 NFs/CMK-3 composite.

To determine the relationship between the current density and operating power of the ternary composite material, we further conducted charge–discharge cycle tests on the electrode at different current densities (1 A, 2 A, 3 A, 4 A, 5 A, 10 A, 20 A, 30 A, 40 A, 50 A), as shown in Figure S10, and based on these results, a corresponding Ragone plot was constructed to illustrate the variation in energy and power density, as presented in Figure 8.

As can be clearly seen from the plot, the energy density of the pure CMK-3 electrode drops significantly under high-current conditions, indicating that the material quickly loses its ability to store energy when given a large current. The CeO₂ NFs/CMK-3 electrode shows good stability, and even when the power density reaches 2500 W/kg, it still maintains a very good energy density (26.39 Wh/kg). The cycle stability of the SiO₂/CeO₂/CMK-3 electrode was evaluated at a current density of 5 A/g, and the results are shown in Figure S11. During the initial cycles, the capacitance % increases due to the improved electrolyte wetting, activation of sites, and enhanced ion transport within the electrode. After 3000 charge–discharge cycles, the electrode exhibited a capacitance retention of 91.98%, demonstrating good long-term stability and durability. Furthermore, EIS analysis of the CeO₂ NFs/SiO₂-100/CMK-3 composite electrode, as shown in Figure S12, provides valuable insights into the electrode's charge transfer resistance. Before cycling, the charge transfer resistance (R_{ct}) is approximately 19 Ω , which slightly increases to 21 Ω after cycling, suggesting negligible structural degradation or material agglomeration during cycling. The SiO₂/CeO₂/CMK-3 ternary composite material further improves its electrochemical performance, and the results are better than CeO₂/CMK-3 and SiO₂/CMK-3, which again illustrates the synergistic effect of SiO₂ and CeO₂.

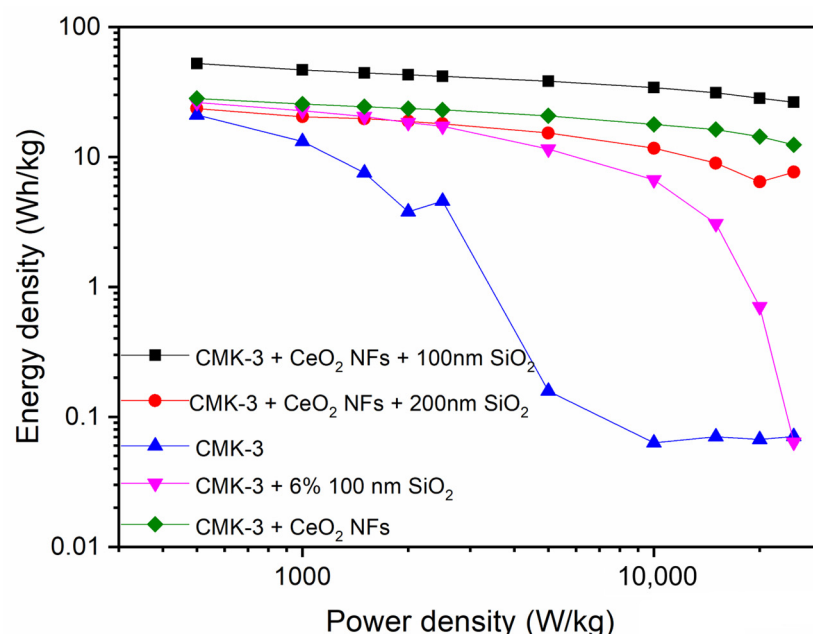


Figure 8. Ragone plot of CMK-3, CeO₂/CMK-3, and CeO₂/SiO₂/CMK-3 electrodes.

4. Conclusions

This research explored the development of high-performance supercapacitor electrodes based on CeO₂/SiO₂/CMK-3 composites. Through a systematic investigation of different CeO₂ morphologies (microparticles and nanofibers), loading ratios, and the incorporation of silica, the electrochemical performance was optimized. The CeO₂ NFs/CMK-3 composite exhibited superior capacitance (403 F/g at 1 A/g) compared to its microparticle counterpart, attributed to its higher surface area and improved dispersion. The addition of SiO₂ nanospheres further enhanced the electrochemical performance, with the SiO₂/CeO₂/CMK-3 electrode achieving a capacitance retention of 91.98% after 3000 cycles at 5 A/g. Additionally, the composite maintained a high energy density of 26.39 Wh/kg at a power density of 2500 W/kg, demonstrating excellent stability under high-current cycling. Furthermore, the addition of silica demonstrated a synergistic effect, further enhancing the

overall performance. These findings provide valuable insights for future research on the design of advanced supercapacitor electrodes.

Supplementary Materials: The following supporting information can be downloaded at: <https://www.mdpi.com/article/10.3390/pr13061766/s1>, Figure S1: SEM image of (a) SiO₂-100 and (b) SiO₂-200; Figure S2: XRD patterns of image of CeO₂ NFs/SiO₂-100/CMK-3; Figure S3: Charge–discharge curves of SBA-15/CMK-3 composite electrodes with different SBA-15 ratios; Figure S4: Water contact angle measurements of SBA-15/CMK-3 composite electrodes with different SBA-15 ratios: (a) 1%, (b) 2%, (c) 4%, (d) 6%, (e) 8%, (f) 10%, (g) 15%; Figure S5: Charge–discharge curves of CeO₂ MPs/CMK-3 composite electrodes; Figure S6: Elemental mapping percentage of CeO₂ MPs/CMK-3 and CeO₂ NFs /CMK-3 composite electrodes; Figure S7: Charge–discharge curves of CeO₂ NFs/CMK-3 composite electrodes; Figure S8: SEM images of (a) CeO₂ NFs/SiO₂-100/cmk-3 and (b) CeO₂ NFs/SiO₂-200/CMK-3; Figure S9: Charge–discharge curves of ternary composite electrodes: (a) CeO₂ NFs/SiO₂-100/CMK-3; (b) CeO₂ NFs/SiO₂-200/CMK-3; Figure S10. Charge-discharge curves of ternary composite electrode at different current density (1–50 A/g); Figure S11: Cyclic stability of CeO₂ NFs/SiO₂-100/CMK-3 composite electrodes at 5 A/g for 3000 cycles; Figure S12: EIS analysis of CeO₂ NFs/SiO₂-100/CMK-3 composite electrodes.

Author Contributions: Conceptualization and data curation, C.-C.C.; methodology and resources, A.-Y.L. and M.-L.T.; writing—original draft preparation, C.-C.C. and A.-Y.L.; writing—review, formal analysis, visualization, and editing, C.K.; supervision, A.-Y.L.; funding acquisition, M.-L.T. All authors have read and agreed to the published version of the manuscript.

Funding: This research was funded by the NSTC, grant numbers NSTC 111-2221-E-003-035-MY3; NSTC 111-2811-E-167-001-MY3.

Data Availability Statement: The original contributions presented in this study are included in the article/Supplementary Materials. Further inquiries can be directed to the corresponding authors.

Acknowledgments: The authors would like to thank the National Science and Technology Council of the Republic of China, Taiwan, for financially supporting this. The authors also thank the Green Energy and Engineering Materials Research Center of the National Chin-Yi University of Technology (NCUT) for the support with material characterization.

Conflicts of Interest: The authors declare no conflicts of interest.

References

1. Reenu; Sonia; Phor, L.; Kumar, A.; Chahal, S. Electrode materials for supercapacitors: A comprehensive review of advancements and performance. *J. Energy Storage* **2024**, *84*, 110698. [CrossRef]
2. Dissanayake, K.; Kularatna-Abeywardana, D. A review of supercapacitors: Materials, technology, challenges, and renewable energy applications. *J. Energy Storage* **2024**, *96*, 112563. [CrossRef]
3. Koventhan, C.; Lo, A.-Y. Morphology engineering of novel MnMoO₄@NiMoO₄ core–shell nanostructure as an electrode material for asymmetric supercapacitor device. *Chem. Eng. J.* **2024**, *485*, 149950. [CrossRef]
4. Zhang, M.; Wang, G.; Lu, L.; Wang, T.; Xu, H.; Yu, C.; Li, H.; Tian, W. Improving the electrochemical performances of active carbon-based supercapacitors through the combination of introducing functional groups and using redox additive electrolyte. *J. Saudi Chem. Soc.* **2018**, *22*, 908–918. [CrossRef]
5. Yumak, T.; Bragg, D.; Sabolsky, E.M. Effect of synthesis methods on the surface and electrochemical characteristics of metal oxide/activated carbon composites for supercapacitor applications. *Appl. Surf. Sci.* **2019**, *469*, 983–993. [CrossRef]
6. Yang, Z.; Ren, J.; Zhang, Z.; Chen, X.; Guan, G.; Qiu, L.; Zhang, Y.; Peng, H. Recent advancement of nanostructured carbon for energy applications. *Chem. Rev.* **2015**, *115*, 5159–5223. [CrossRef]
7. Senthilkumar, S.T.; Fu, N.; Liu, Y.; Wang, Y.; Zhou, L.; Huang, H. Flexible fiber hybrid supercapacitor with NiCo₂O₄ nanograss@carbon fiber and bio-waste derived high surface area porous carbon. *Electrochim. Acta* **2016**, *211*, 411–419. [CrossRef]
8. Chen, X.; Paul, R.; Dai, L. Carbon-based supercapacitors for efficient energy storage. *Natl. Sci. Rev.* **2017**, *4*, 453–489. [CrossRef]
9. Hakamada, M.; Abe, T.; Mabuchi, M. Electrodes from carbon nanotubes/NiO nanocomposites synthesized in modified Watts bath for supercapacitors. *J. Power Sources* **2016**, *325*, 670–674. [CrossRef]

10. Chung, Y.-C.; Julistian, A.; Saravanan, L.; Chen, P.-R.; Xu, B.-C.; Xie, P.-J.; Lo, A.-Y. Hydrothermal Synthesis of CuO/RuO₂/MWCNT Nanocomposites with Morphological Variants for High Efficient Supercapacitors. *Catalysts* **2022**, *12*, 23. [\[CrossRef\]](#)
11. Lo, A.-Y.; Saravanan, L.; Tseng, C.-M.; Wang, F.-K.; Huang, J.-T. Effect of Composition Ratios on the Performance of Graphene/Carbon Nanotube/Manganese Oxide Composites toward Supercapacitor Applications. *ACS Omega* **2020**, *5*, 578–587. [\[CrossRef\]](#) [\[PubMed\]](#)
12. Guo, X.; Zheng, S.; Zhang, G.; Xiao, X.; Li, X.; Xu, Y.; Xue, H.; Pang, H. Nanostructured graphene-based materials for flexible energy storage. *Energy Storage Mater.* **2017**, *9*, 150–169. [\[CrossRef\]](#)
13. Hall, P.J.; Mirzaeian, M.; Fletcher, S.I.; Sillars, F.B.; Rennie, A.J.R.; Shitta-Bey, G.O.; Wilson, G.; Cruden, A.; Carter, R. Energy storage in electrochemical capacitors: Designing functional materials to improve performance. *Energy Environ. Sci.* **2010**, *3*, 1238–1251. [\[CrossRef\]](#)
14. Lo, A.-Y.; Chang, C.-C.; Lai, Y.-W.; Chen, P.-R.; Xu, B.-C. Improving the Supercapacitor Performance by Dispersing SiO₂ Microspheres in Electrodes. *ACS Omega* **2020**, *5*, 11522–11528. [\[CrossRef\]](#) [\[PubMed\]](#)
15. Koventhan, C.; Chung, Y.-C.; Lo, A.-Y.; Weng, H.-C.; Hung, W.-H. Development of a polyaniline/CMK-3/hydroquinone composite supercapacitor system. *Mater. Chem. Phys.* **2023**, *297*, 127369. [\[CrossRef\]](#)
16. Miller, E.E.; Hua, Y.; Tezel, F.H. Materials for energy storage: Review of electrode materials and methods of increasing capacitance for supercapacitors. *J. Energy Storage* **2018**, *20*, 30–40. [\[CrossRef\]](#)
17. Zan, G.; Li, S.; Chen, P.; Dong, K.; Wu, Q.; Wu, T. Mesoporous Cubic Nanocages Assembled by Coupled Monolayers with 100% Theoretical Capacity and Robust Cycling. *ACS Cent. Sci.* **2024**, *10*, 1283–1294. [\[CrossRef\]](#)
18. Zheng, S.; Wu, Z.-S.; Wang, S.; Xiao, H.; Zhou, F.; Sun, C.; Bao, X.; Cheng, H.-M. Graphene-based materials for high-voltage and high-energy asymmetric supercapacitors. *Energy Storage Mater.* **2017**, *6*, 70–97. [\[CrossRef\]](#)
19. Vipu Vinayak, V.J.; Deshmukh, K.; Murthy, V.R.K.; Pasha, S.K.K. Conducting polymer based nanocomposites for supercapacitor applications: A review of recent advances, challenges and future prospects. *J. Energy Storage* **2024**, *100*, 113551. [\[CrossRef\]](#)
20. Wu, Z.-S.; Wang, D.-W.; Ren, W.; Zhao, J.; Zhou, G.; Li, F.; Cheng, H.-M. Anchoring Hydrous RuO₂ on Graphene Sheets for High-Performance Electrochemical Capacitors. *Adv. Funct. Mater.* **2010**, *20*, 3595–3602. [\[CrossRef\]](#)
21. Kulal, P.M.; Dubal, D.P.; Lokhande, C.D.; Fulari, V.J. Chemical synthesis of Fe₂O₃ thin films for supercapacitor application. *J. Alloys Compd.* **2011**, *509*, 2567–2571. [\[CrossRef\]](#)
22. Subramanian, V.; Zhu, H.; Vajtai, R.; Ajayan, P.M.; Wei, B. Hydrothermal Synthesis and Pseudocapacitance Properties of MnO₂ Nanostructures. *J. Phys. Chem. B* **2005**, *109*, 20207–20214. [\[CrossRef\]](#) [\[PubMed\]](#)
23. Dong, J.; Wang, Z.; Kang, X. The synthesis of graphene/PVDF composite binder and its application in high performance MnO₂ supercapacitors. *Colloids Surf. A Physicochem. Eng. Asp.* **2016**, *489*, 282–288. [\[CrossRef\]](#)
24. Du, W.; Liu, R.; Jiang, Y.; Lu, Q.; Fan, Y.; Gao, F. Facile synthesis of hollow Co₃O₄ boxes for high capacity supercapacitor. *J. Power Sources* **2013**, *227*, 101–105. [\[CrossRef\]](#)
25. Xu, L.; Xia, J.; Xu, H.; Yin, S.; Wang, K.; Huang, L.; Wang, L.; Li, H. Reactable ionic liquid assisted solvothermal synthesis of graphite-like C₃N₄ hybridized α -Fe₂O₃ hollow microspheres with enhanced supercapacitive performance. *J. Power Sources* **2014**, *245*, 866–874. [\[CrossRef\]](#)
26. Jin, Y.; Jia, M. Design and synthesis of nanostructured graphene-SnO₂-polyaniline ternary composite and their excellent supercapacitor performance. *Colloids Surf. A Physicochem. Eng. Asp.* **2015**, *464*, 17–25. [\[CrossRef\]](#)
27. Qu, Q.; Chen, Z.; Sun, G.-T.; Qiu, L.; Zhu, M.-Q. CoFe₂O₄ nanoparticles as a bifunctional agent on activated porous carbon for battery-type asymmetrical supercapacitor. *Chem. Synth.* **2024**, *4*, 26. [\[CrossRef\]](#)
28. Wu, W.; Qi, W.; Zhao, Y.; Tang, X.; Qiu, Y.; Su, D.; Fan, H.; Wang, G. Hollow CeO₂ spheres conformally coated with graphitic carbon for high-performance supercapacitor electrodes. *Appl. Surf. Sci.* **2019**, *463*, 244–252. [\[CrossRef\]](#)
29. Li, J.; Chen, D.; Wu, Q. Facile synthesis of CoS porous nanoflake for high performance supercapacitor electrode materials. *J. Energy Storage* **2019**, *23*, 511–514. [\[CrossRef\]](#)
30. Wang, T.; Li, K.; An, S.; Song, C.; Guo, X. Facile and green synthesis of TiN/C as electrode materials for supercapacitors. *Appl. Surf. Sci.* **2019**, *470*, 241–249. [\[CrossRef\]](#)
31. Prakash, R.; Kumar, A.; Pandey, A.; Kaur, D. Binder free and high performance of sputtered tungsten nitride thin film electrode for supercapacitor device. *Int. J. Hydrogen Energy* **2019**, *44*, 10823–10832. [\[CrossRef\]](#)
32. Lo, A.-Y.; Jheng, Y.; Huang, T.-C.; Tseng, C.-M. Study on RuO₂/CMK-3/CNTs composites for high power and high energy density supercapacitor. *Appl. Energy* **2015**, *153*, 15–21. [\[CrossRef\]](#)
33. Xu, Z.-H.; Li, X.-L.; Li, Q.-W.; Lv, K.; Liu, J.-S.; Hang, X.-K.; Bayaguud, A. Mechanism research progress on transition metal compound electrode materials for supercapacitors. *Rare Metals* **2024**, *43*, 4076–4098.
34. Das, H.T.; Tamilarasan, E.B.; Dutta, S.; Das, N.; Das, P.; Mondal, A.; Imran, M. Recent trend of CeO₂-based nanocomposites electrode in supercapacitor: A review on energy storage applications. *J. Energy Storage* **2022**, *50*, 104643.

35. Nguyen, H.T.T.; Ohtani, M.; Kobihiro, K. One-pot synthesis of SiO₂–CeO₂ nanoparticle composites with enhanced heat tolerance. *Microporous Mesoporous Mater.* **2019**, *273*, 35–40. [[CrossRef](#)]
36. Phokha, S.; Hunpratub, S.; Usher, B.; Pimsawat, A.; Chanlek, N.; Maensiri, S. Effects of CeO₂ nanoparticles on electrochemical properties of carbon/CeO₂ composites. *Appl. Surf. Sci.* **2018**, *446*, 36–46.
37. Wang, Y.; Guo, C.X.; Liu, J.; Chen, T.; Yang, H.; Li, C.M. CeO₂ nanoparticles/graphene nanocomposite-based high performance supercapacitor. *Dalton Trans.* **2011**, *40*, 6388–6391.
38. Ho, M.-C.; Chao, C.-H.; Lo, A.-Y.; Chen, C.-H.; Wu, R.-J.; Tsai, M.-H.; Huang, Y.-C.; Whang, W.-T. Significant improvement in the thermoelectric properties of zwitterionic polysquaraine composite films. *Mater. Chem. Phys.* **2013**, *141*, 920–928.
39. Prasanna, K.; Santhoshkumar, P.; Jo, Y.N.; Sivagami, I.N.; Kang, S.H.; Joe, Y.C.; Lee, C.W. Highly porous CeO₂ nanostructures prepared via combustion synthesis for supercapacitor applications. *Appl. Surf. Sci.* **2018**, *449*, 454–460.

Disclaimer/Publisher’s Note: The statements, opinions and data contained in all publications are solely those of the individual author(s) and contributor(s) and not of MDPI and/or the editor(s). MDPI and/or the editor(s) disclaim responsibility for any injury to people or property resulting from any ideas, methods, instructions or products referred to in the content.